Absolute values of gravity wave momentum flux derived from satellite data

Manfred Ern and Peter Preusse
Institute for Chemistry and Dynamics of the Geosphere I, Forschungszentrum Jülich, Jülich, Germany

M. Joan Alexander
Colorado Research Associates, Boulder, Colorado, USA

Christopher D. Warner
Centre for Atmospheric Sciences, University of Cambridge, Cambridge, UK

Received 10 March 2004; revised 18 June 2004; accepted 20 July 2004; published 19 October 2004.

[1] Temperature data obtained by the Cryogenic Infrared Spectrometers and Telescopes for the Atmosphere (CRISTA) are analyzed for gravity waves (GWs). Amplitude, phase and vertical wavelength are determined from detrended temperature height profiles. The retrieved phases are utilized to estimate the horizontal wavelengths. At 25 km altitude an equatorial maximum of horizontal wavelength with a decrease toward mid and high latitudes is found. Simultaneous estimates of both horizontal and vertical wavelengths and temperature amplitudes allow the direct calculation of GW momentum flux (MF) from satellite observations for the first time. However, histograms of horizontal wavelength distributions indicate severe undersampling which prevents the retrieval of the propagation directions of the waves, and suggests our MF estimates may be too low, particularly at the high latitudes. Therefore an empirical aliasing correction has been applied. A world map of MF at 25 km altitude shows high variability and pronounced source regions and deviates in structure from a map of GW variances at the same altitude. Results from the Warner and McIntyre GW parameterization scheme (three-part model) show better agreement with CRISTA MF estimates than with CRISTA squared GW amplitudes. Best agreement is found for low model launch levels. Large error ranges of the estimated MF values obtained in this paper could be substantially reduced by improved horizontal sampling in future satellite missions. *INDEX TERMS:* 3384 Meteorology and Atmospheric Dynamics: Waves and tides; 0394 Atmospheric Composition and Structure: Instruments and techniques; 3319 Meteorology and Atmospheric Dynamics: General circulation; 3334 Meteorology and Atmospheric Dynamics: Middle atmosphere dynamics (0341, 0342); *KEYWORDS:* gravity waves, momentum flux, satellite remote sensing

Citation: Ern, M., P. Preusse, M. J. Alexander, and C. D. Warner (2004), Absolute values of gravity wave momentum flux derived from satellite data, *J. Geophys. Res.*, *109*, D20103, doi:10.1029/2004JD004752.

1. Introduction

[2] The importance of gravity waves (GWs) for the dynamics of the middle atmosphere is widely accepted [*McLandress*, 1998; *McIntyre*, 1998; *Holton and Alexander*, 2000]. Short and mesoscale GWs contribute largely to the momentum balance of the stratosphere and dominate in the mesosphere. In addition, the quasibiennial and semiannual oscillations in equatorial zonal winds are at least partially driven by the convergence of momentum flux (MF) carried by GWs [*Dunkerton*, 1997; *Garcia and Sassi*, 1999; *Mayr et al.*, 1998; *Scaife et al.*, 2000; *Giorgetta et al.*, 2002]. However, the GW parameterization schemes used in global circulation models (GCMs) are still based on important simplifying assumptions [*Hines*, 1997; *Warner and McIntyre*, 1999; *Medvedev and Klaassen*, 2000] and have a number of freely adjustable parameters (e.g., the model launch level). Estimates of the MF still rely more on models than on measurements. Therefore an experimental validation of the GW MF calculated by models is an important issue.

[3] Recently an increasing number of satellite instruments have been evaluated for GWs. GW climatologies based on zonal mean values have been published for the Limb Infrared Monitor of the Stratosphere (LIMS) [*Fetzer and Gille*, 1994], which was flown on the Nimbus-7 satellite and made measurements from Oct. 1978 until May 1979. Climatologies were also made for the Microwave Limb Sounder (MLS) on board the Upper Atmosphere Research Satellite (UARS) [*Wu and Waters*, 1996a, 1996b, 1997; *McLandress et al.*, 2000; *Wu*, 2001], the meteorological program of the Global Positioning System (GPS/MET) [*Tsuda et al.*, 2000], and the Cryogenic Infrared Spectrometers and Telescopes for the Atmosphere (CRISTA) [*Preusse*

0148-0227/04/2004JD004752

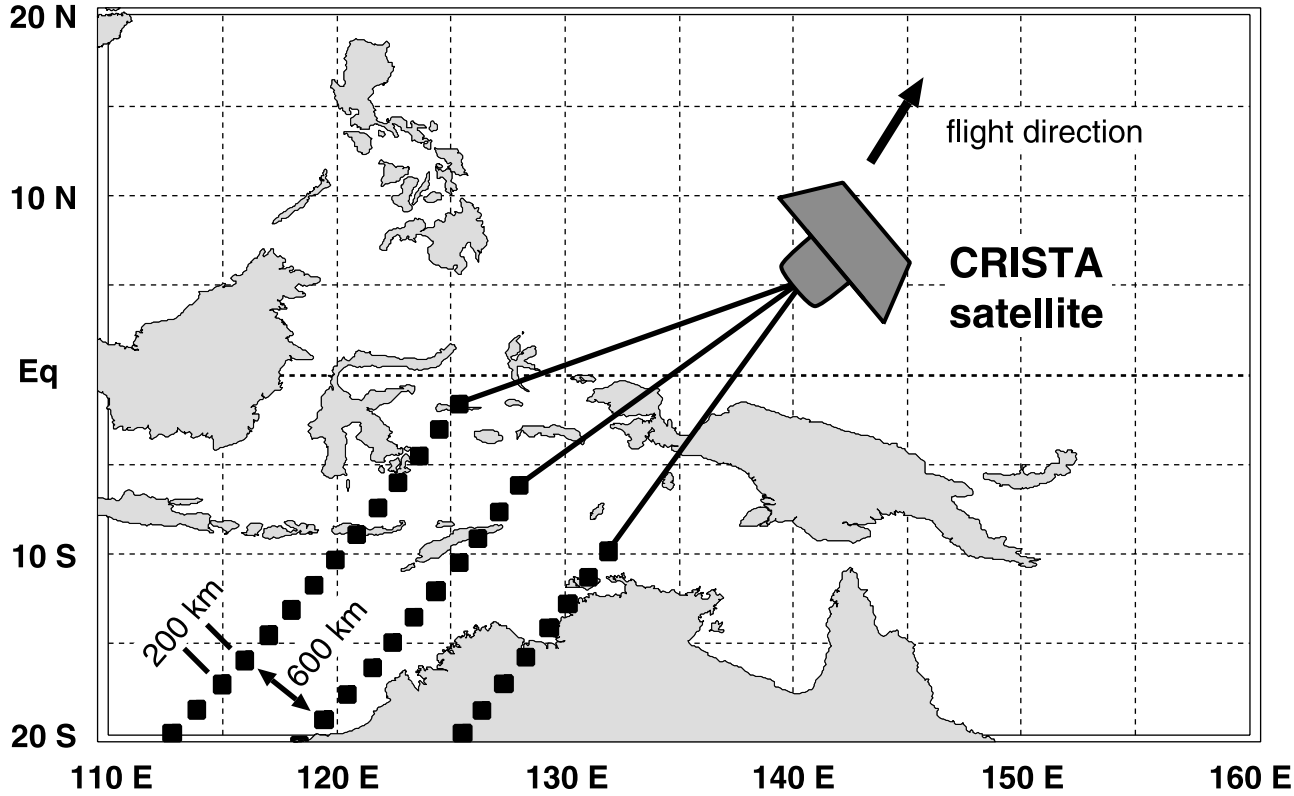

Figure 1. Measurement geometry of the CRISTA instrument. Each square represents a full altitude profile of temperature and several trace gases. Using three viewing directions results in three tracks of altitude profiles measured simultaneously. For details, see text.

et al., 1999, 2000, 2002] on two shuttle missions in 1994 and 1997. These climatologies are all based on gravity wave temperature variances and, in most cases, give estimates of either horizontal or vertical wavelengths. However, none of these analyses have provided simultaneous estimates of both horizontal and vertical wavelength, so they cannot be used to estimate intrinsic frequency and MF.

[4] In this paper we present an algorithm to determine the horizontal as well as the vertical wavelength of individual waves (section 3) after briefly introducing the CRISTA experiment (section 2). The inferred horizontal wavelength distributions have implications for the vertical flux of horizontal momentum presented in section 4. In section 5 the MF distribution obtained from CRISTA data is compared to results from the Warner and McIntyre GW parameterization. Finally, section 6 discusses how, despite apparent shortcomings of current datasets, new insights can be obtained.

2. Instrument and Data

[5] The CRISTA instrument [*Offermann et al.*, 1999] was flown on two Shuttle missions in November 1994 and August 1997 providing one week of data for each flight. CRISTA is a limb scanning instrument which measures thermal emissions of atmospheric trace gases in the mid infrared. Stratospheric temperatures were retrieved from a 12.6 μm CO_2 Q-branch [*Riese et al.*, 1999] with an accuracy of 2 K and a precision of 0.4 K. By scanning the atmosphere with three telescopes simultaneously, CRISTA achieved high spatial resolution in all three dimensions. The vertical scanning step is 1.5 km for CRISTA-1 and 2.0 km for CRISTA-2.

[6] Figure 1 shows the measurement geometry of the CRISTA instrument. Using three viewing directions simultaneously results in three tracks of altitude profiles (indicated as squares in Figure 1). The lateral viewing directions are 18° apart from the center viewing direction. In Figure 1 the along-track distance between subsequent altitude profiles of a single telescope is 200 km.

[7] During both missions, two main measuring modes were performed, one focusing on the stratosphere, the other extending scans up to the lower mesosphere. Extending the scan range implies a larger horizontal distance along track. The along-track separation of altitude scans is 200 km in the stratospheric and 400 km in the mesospheric scan modes for CRISTA-1 and 240 and 480 km for CRISTA-2. The distance between simultaneously measured profiles across the line of sight (LOS) is 600 km. This is also the distance between the three ground tracks when the instrument looks backward, as during CRISTA-1 (also see Figure 1). Detailed descriptions of the sampling patterns can be found in *Riese et al.* [1999] and *Grossmann* [2000].

[8] The basic analysis method for retrieving GWs from CRISTA temperatures is described in depth by *Preusse et al.* [2002]. In this paper we will therefore only give a very brief overview. To isolate GWs from the background atmosphere and planetary waves CRISTA temperature data are detrended by a wavenumber 0–6 Kalman filter eliminating zonal wavenumbers $\leq$6. Individual vertical profiles of the detrended temperature data (residual temperatures)

were analyzed using the Maximum Entropy Method (MEM) and harmonic analysis (HA). The MEM spectrum was calculated using the complete height profile. The MEM spectral peaks were used to constrain harmonic fits to the profile within a 10 km or 14 km altitude window that was moved upward in increments of 1.5 km for CRISTA-1 and of 2 km for CRISTA-2. The full height range is covered by the analysis. This MEM/HA analysis provides height profiles of amplitudes, phases and vertical wavelengths of the two largest oscillations in any given profile, and allows these values to vary with height. The vertical wavelength range covered is 5 km $< \lambda_z <$ 25 km for CRISTA-1 and 6 km $< \lambda_z <$ 30 km for CRISTA-2, respectively. The lower limit is defined by the instruments sensitivity and the higher value by the MEM/HA analysis.

3. Horizontal Wavelength Analysis

[9] Horizontal wavelength analyses are frequently performed on subsets of orbit track data taken at fixed altitudes. Standard analysis methods such as Fourier transform or autocorrelation are applied to these subsets [*Fetzer and Gille*, 1994; *Eidmann et al.*, 2001; *Wu*, 2001; *Eidmann et al.*, 2002]. Both these methods require the wave field to be nearly homogeneous, at least for the sampling interval considered. Moreover, these statistical analyses require of the order of 10 sampling points at least. For CRISTA this is equivalent to an interval length of more than 2000 km.

[10] Recent case studies have shown that coherent wave structures often extend only 600 km or less [*Preusse et al.*, 2001, 2002]. Therefore, given a horizontal sampling of 200 km, along-track standard analysis methods cannot be expected to capture these waves properly. In addition, a large fraction of the waves probably have wavelengths well below the Nyquist wavelength of 400 km.

[11] Based on sensitivity studies, *Preusse et al.* [2002] have shown that waves with horizontal wavelengths of $\sim$100 km can be detected by CRISTA. In a case study [*Preusse et al.*, 2002] a wave with a horizontal wavelength of 130 km was inferred from several overpasses of the same region. The short horizontal wavelength below the Nyquist wavelength was further supported by three different GW models. This demonstrates that CRISTA data contain variations from waves with horizontal wavelengths below the sampling distance. Aliasing and the low spatial extent of individual GW events therefore indicate that in the horizontal direction the coverage is at best sparse.

[12] In the vertical direction, however, no aliasing effects are possible because the retrieval process suppresses all structures with vertical wavelengths shorter than the vertical sampling distance [*Preusse et al.*, 2002]. Thus, if we can find a method to use the results of the vertical analysis for a nonstationary analysis method, we might be able to overcome the aforementioned problems, at least in part.

[13] We will make an attempt to deduce the horizontal wavelength from two or more adjacent profiles by assuming that these profiles belong to the same sinusoidal wave. This assumption is obviously sometimes violated and cases will be discussed in detail below. A single sinusoidal wave can be written as

$$T'(x_h, z, t) = \hat{T}(z)\sin(k_h x_h + mz - \omega t + \psi) \quad (1)$$

where $\hat{T}$ denotes the temperature amplitude, x_h is the horizontal coordinate, $k_h = 2\pi/\lambda_h$ is the horizontal wavenumber, $m = 2\pi/\lambda_z$ is the vertical wavenumber, and $\omega = 2\pi/\tau$ is the ground-based, or absolute, frequency.

[14] Since the minimum horizontal wavelength visible to CRISTA is limited by the measuring geometry ($\lambda_h >$ 100 km) and given that we only consider vertical wavelengths less than 30 km (see section 3.2), there exists also a minimum period of about 20 min. Since the satellite moves at 8 km/s, even a wave packet of the size of a few 1000 km would be measured in just a few minutes. The wave can therefore be considered to have been measured instantaneously if data from a single satellite overpass are used.

[15] Using the MEM/HA technique we determine the phase $\phi(x_h, z) = k_h x_h + mz + \psi$ for every measured height profile at the altitude level considered. Since z is fixed, the horizontal wavenumber k_h along the connecting line between two adjacent profiles i and j can be deduced from the phases ϕ of these profiles:

$$k_h = \frac{\partial\phi(x_h)}{\partial x_h} = \frac{\Delta\phi_{i,j}}{\Delta x_{i,j}} \quad (2)$$

3.1. Along-Track Analysis

[16] The simplest method is to apply (2) to profiles measured along the orbit track. To calculate the distance $\Delta x_{i,j}$ the precise locations from the satellite attitude control are utilized. We calculate the horizontal wavelength, the mean vertical wavelength, the difference of the two vertical wavelengths, and the distance along the orbit track. The vertical wavelength difference is used as a criterion indicating whether adjacent profiles really belong to the same wave system.

[17] However, the method is limited in two ways. First, due to the observational horizontal wavelength limit of $\sim$100 km [*Preusse et al.*, 2002], which is independent of the sampling distance, observed waves might have horizontal wavelengths too short to be resolved properly by the horizontal sampling of the satellite. Given a horizontal sampling distance Δx_h between two altitude profiles considered we are only able to assign the correct horizontal wavelength to waves with wavelengths longer than the Nyquist wavelength given by twice the sampling distance: $\lambda_{h,N} = 2\Delta x_h$. Otherwise aliasing effects will appear as the waves are not sampled sufficiently. If in a region all wave events are sampled insufficiently on average the measured phase differences are random and distributed uniformly. Similarly, if adjacent profiles exhibit fluctuations stemming from different waves, random equally distributed phase differences will also result. In further analyses we will discuss zonal or regional mean distributions.

[18] This implies the question: which average wavenumber is observed if the wave field consists entirely of GWs at or near the short horizontal wavelength edge of the CRISTA sensitivity? In this case the wavelengths are notably shorter than the sampling distance and the phases indeed appear random. Consider the average of the absolute value of the wavenumber in the case of a random phase distribution and neglect the direction. Here, although the real phase difference in the atmosphere might be larger, measured phase differences $\Delta\phi$ are always in the interval $[-\pi, \pi]$, since a

phase difference larger than π would lead to a wavelength below the Nyquist wavelength. Such aliasing problems are frequently discussed in the literature [*Press et al.*, 1992; *Salby*, 1983]. Neglecting the direction, the mean wavenumber is equally distributed in the interval $[0, k_{h,\max}] = [0/\Delta x_h, \pi/\Delta x_h]$ because of the assumed random phase distribution, and the mean value is $\breve{k}_h = \pi/2\Delta x_h$ corresponding to a wavelength of $\breve{\lambda}_h = 4 * \Delta x_h$, twice the Nyquist wavelength. If a large part of the wave spectrum is below the Nyquist wavelength, $\breve{\lambda}_h$ is the minimum mean value to be observed. Since we assume that short horizontal wavelengths are always present in the atmosphere, this is the minimum wavelength which can be expected in a mean value of a large sample such as a zonal mean.

[19] The second way the method is limited is that only the apparent wavelengths along the orbit track are observed. These are in general longer than the real wavelengths. For example, the waves at the equator might preferentially propagate in the east-west direction. Since the orbit track intersects the equator at an angle of 57° the wavelengths would in this case appear to be a factor $1/\cos(57°) \simeq 1.8$ longer.

3.2. Results of the Horizontal Wavelength Analysis

[20] The shape of the horizontal wavenumber distribution at 25 km altitude is investigated in Figure 2. Histograms are shown for different latitude regions during CRISTA-2 using only those pairs of altitude profiles with vertical wavelength difference lower than 6 km to ensure that the same wave system is observed. For better comparison the values given at the *x* axes in Figure 2 are horizontal wavelengths, but the axes are scaled to be linear in horizontal wavenumber to show the shape of the horizontal wavenumber distribution of the data investigated.

[21] Figure 2a shows the distribution for tropical latitudes from 15°S to 15°N. The distribution is dominated by long wavelengths (short wavenumbers) indicating that most of the waves can be resolved by the satellite sampling. Figure 2b shows the distribution of horizontal wavelengths at high northern latitudes from 50°N–70°N between 30°W and 90°W. The distribution is nearly homogeneous, except for the shortest wavelengths, 400–500 km, where a small decrease is observed. As already discussed in section 3.1, a homogeneous distribution is to be expected if most of the observed waves have wavelengths shorter than the Nyquist wavelength and so are severely undersampled. Severe undersampling might not be the only reason for a homogeneous distribution; however, this appears to be the most likely explanation. In particular, evidence from a case study of mountain waves above South America based on CRISTA-1 data [*Preusse et al.*, 2002] observed undersampling and the corresponding horizontal wavelength distribution was homogeneous and very similar to Figure 2b. The distribution for the southern midlatitudes from 40°S–60°S shown in Figure 2c is intermediate between the homogeneous distribution of Figure 2b and the increase at long wavelengths of Figure 2a. This suggests that some of the waves have short horizontal wavelengths but that additional waves with long horizontal wavelengths exist.

[22] Figure 3c shows the global distribution of horizontal wavelengths at an altitude of 25 km. Horizontal wavelengths are maximum in the southern tropics (20°S–0°N). Following *Alexander et al.* [2002], there are two reasons why an equatorial maximum of horizontal wavelength would indeed be expected.

[23] First, the intrinsic wave frequency $\hat{\omega}$ is limited by the Coriolis parameter f to $\hat{\omega} > f = 2\Omega \sin(\Phi)$, where Ω is the Earth rotation frequency and Φ is the latitude. At the equator $f \rightarrow 0$ so this limitation vanishes and low frequency waves are allowed. Since the energy spectrum of gravity waves can be assumed to be proportional to $\hat{\omega}^{-p}$ with p = 5/3 [e.g., *Warner and McIntyre*, 1996] there is a higher probability for low frequency waves to exist, if they are allowed to. Therefore at the equator the distribution may be dominated by the very low frequency waves. The dispersion relation (3) valid in the midfrequency approximation ($N \gg \hat{\omega} \gg f$):

$$\hat{\omega}^2 = \frac{N^2 k_h^2}{m^2} \tag{3}$$

with k_h being the horizontal wavenumber and N the buoyancy frequency suggests that low frequency waves will tend to have longer horizontal wavelengths just as is seen in Figure 3c for the mean horizontal wavelength.

[24] Second, *Alexander et al.* [2002] argue that the vertical group speed of a GW is a function of $\hat{\omega}$ and becomes slower with lower $\hat{\omega}$. Wherever wave sources are intermittent in space and time, these low frequency waves will dominate observations in the lower stratosphere near their sources simply because of their slow vertical propagation and correspondingly high "probability of observation".

4. Momentum Flux Estimation

[25] As summarized in section 1, GW MF is a key quantity for understanding middle atmosphere dynamics and is therefore most urgently in need of validation by measurements. Our technique for retrieving temperature amplitude and horizontal and vertical wavelengths of individual monochromatic GWs allows us to estimate the MF of the measured waves.

[26] An equation for the vertical flux of horizontal momentum can be derived starting from equation (41) in *Fritts and Alexander* [2003] giving the x- and y-components of the MF vector

$$\left(F_{px}, F_{py}\right) = \bar{\varrho}\left(1 - \frac{f^2}{\hat{\omega}^2}\right)\left(\overline{u'w'}, \overline{v'w'}\right) \tag{4}$$

valid for conservative propagation of the waves. The vector (u', v', w') is the vector of wind perturbations. Further, the polarization relations between the perturbation amplitudes given in the same paper have been used. Then the total vertical flux of horizontal momentum due to GWs

$$F_{ph} = \sqrt{F_{px}^2 + F_{py}^2} \tag{5}$$

has been calculated (see also appendix A) and we obtain

$$\begin{aligned} F_{ph} = &\left[1 - \frac{\hat{\omega}^2}{N^2}\right] \times \left[1 + \frac{1}{m^2}\left(\frac{1}{2H} - \frac{g}{c_s^2}\right)^2\right]^{-1} \\ &\times \left[1 + \left(\frac{f}{m\hat{\omega}}\right)^2 \left(\frac{1}{2H} - \frac{g}{c_s^2}\right)^2\right]^{1/2} \\ &\times \frac{1}{2}\bar{\varrho}\frac{k_h}{m}\left(\frac{g}{N}\right)^2 \left(\frac{\hat{T}}{T}\right)^2 \end{aligned} \tag{6}$$

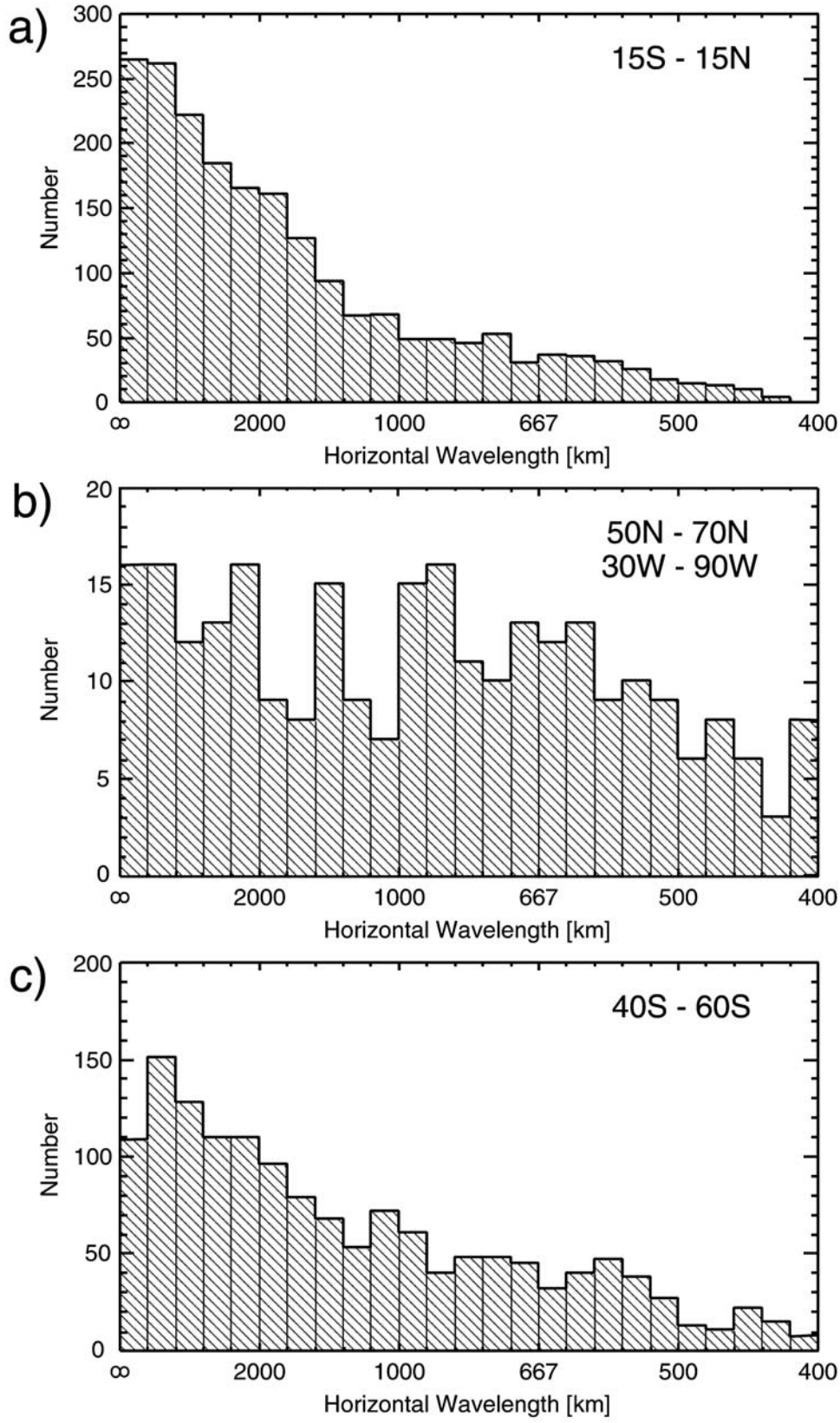

Figure 2. Histograms showing the horizontal wavenumber distribution for pairs of CRISTA-2 (August 1997) altitude profiles with vertical wavelength difference lower than 6 km. For better comparison the values given at the *x* axes are horizontal wavelengths, but the axes are scaled to be linear in horizontal wavenumber. (a) Tropical latitudes (15°S–15°N), (b) northern high latitudes (50°N–70°N between 30°W and 90°W), and (c) southern mid and high latitudes (40°S–60°S). For details, see text.

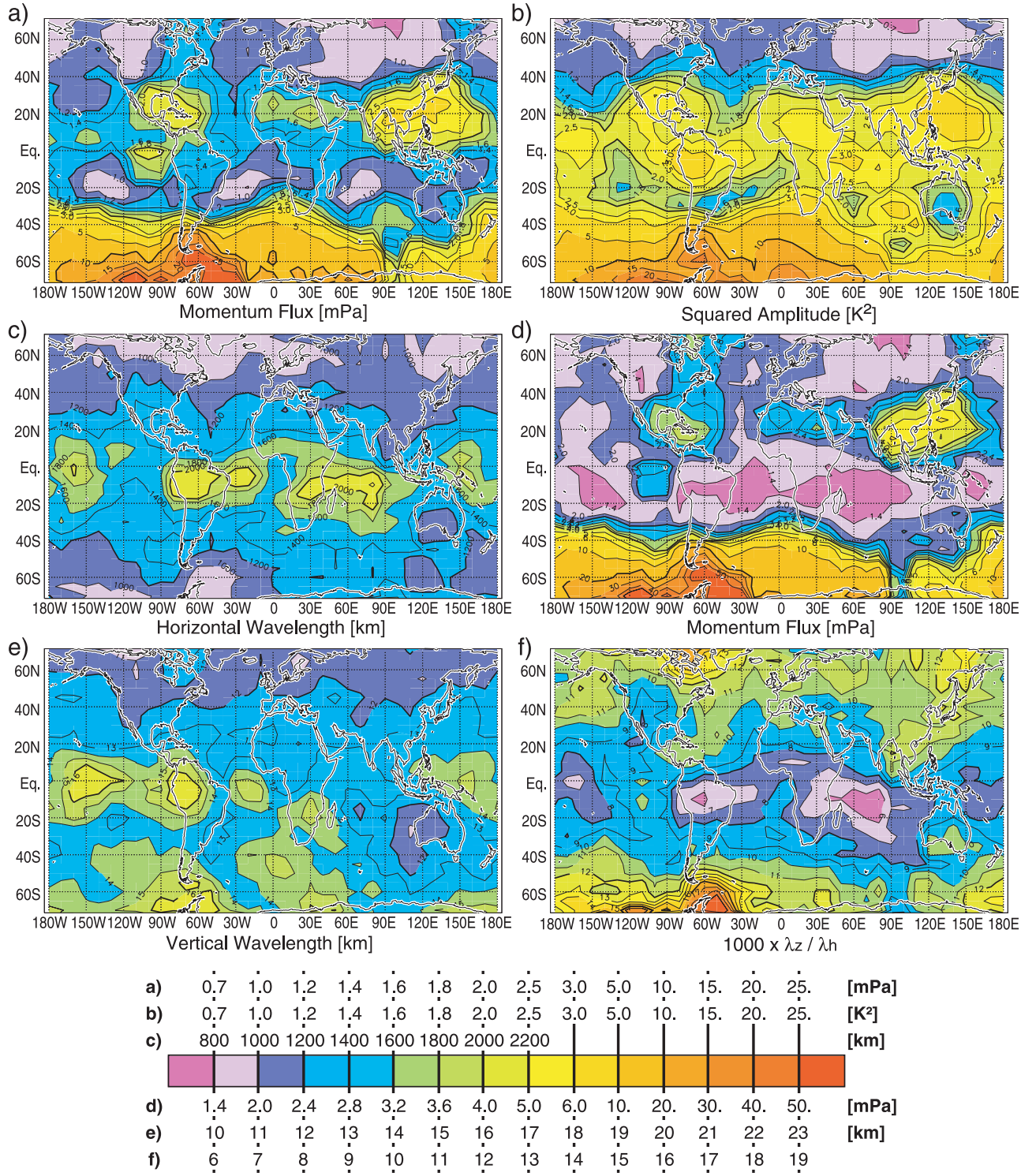

Figure 3. For CRISTA-2 (August 1997) at 25 km altitude: (a) absolute values of the vertical flux of horizontal momentum due to GWs, (b) squared GW temperature amplitudes of the same data, (c) average horizontal wavelengths, (d) same as Figure 3a, but with a correction for aliasing effects applied, (e) average vertical wavelengths, and (f) the average ratio of vertical and horizontal wavelength. Comparison of Figures 3a and 3b with the average horizontal (Figure 3c) and vertical (Figure 3e) wavelengths as well as their average ratio (Figure 3f) shows that structures were enhanced mainly in regions of short horizontal wavelengths, e.g., along the East Asian coastline and above the Antarctic Peninsula. In contrast, the southern tropics (20°S to equator) are substantially weakened. This is further amplified if a correction is made for aliasing (Figure 3d).

where $\hat{T}$ is the temperature amplitude of the wave, k_h is the horizontal wavenumber, $\bar{\varrho}$ the background atmosphere density.

[27] In equation (6) the deviation of the three terms in squared brackets from unity defines the deviation from the midfrequency approximation which typically is less than ~10% for CRISTA observations. In the midfrequency approximation one can easily express $\hat{\omega}$ by k_h via the dispersion relation (3) and relate the MF to the potential energy

$$F_{ph} = \frac{1}{2}\varrho\frac{k_h}{m}\left(\frac{g}{N}\right)^2\left(\frac{\hat{T}}{T}\right)^2 = \frac{k_h}{m}E_{pot} \tag{7}$$

[28] Although (7) shows that, in principle, MF can be directly calculated from temperature profiles taken by a satellite, the remaining uncertainties are still huge for the current generation of instruments. For example, the histogram for northern high latitudes in Figure 2b indicates that a large fraction of the observed waves have wavelengths around or below the Nyquist frequency. This being the case we cannot infer the horizontal wavelength of individual wave events. Worse, the direction of the wave propagation, i.e., the direction of the wavevector $\mathbf{k}_h$ whose magnitude is k_h, remains unknown. A good example that illustrates these difficulties are three consecutive profiles measured above the Andes at the southern tip of South America which show a very pronounced mountain wave structure [*Eckermann and Preusse*, 1999; *Preusse et al.*, 2002]. By a number of arguments it can be shown that these waves have a wavelength of ~130 km, but appear to have ~400 km wavelength because of the sampling distance. Applying (7) to the output of our along-track analysis (section 3.1) for a 400 km wavelength, rather than a 130 km wavelength, would underestimate the MF by a factor of 3. In a vertical cross section, mountain waves always have phase fronts tilted against the prevailing wind and the deposited momentum decelerates the background wind field. Since in this example the Nyquist wavelength is very close to an integer multiple of the mountain wave wavelength, the first two profiles imply the correct phase tilt whereas from the second and third profile a phase tilt in the direction of the background wind would be inferred. Aliasing effects will be further discussed in sections 4.2 and 4.3.

4.1. Geographical Variation of Momentum Flux

[29] To calculate global maps of MF we neglect direction and calculate absolute values of the MF directly from the individual profile pairs. Only two constraints are applied. First, the difference $\Delta\lambda_z$ of the two vertical wavelengths in a data pair has to be smaller than 6 km to make sure that the same wave system is observed. This is a weak constraint because only a small part of profile pairs is filtered out this way. Second, we only consider profile pairs of standard stratospheric sampling distance ($\Delta x \approx 240$ km for CRISTA-2).

[30] Also we apply different "visibility corrections" for short and long horizontal wavelengths. Due to radiative transport and retrieval effects the sensitivity of CRISTA to different vertical and horizontal wavelength is always lower than 1 [*Preusse et al.*, 2002]. At vertical wavelengths shorter than ~10 km the signal degradation is caused primarily by vertical sampling and retrieval and is hence independent of the horizontal wavelength. At long vertical wavelength ($\lambda_z > 15$ km) the sensitivity is reduced due to the viewing geometry, i.e., the variation of wave phase along the limb ray. Depending on horizontal wavelength along LOS, the sensitivity can vary between 0.5 and 1.

[31] We account for this dependence on horizontal wavelength by dividing the range of horizontal wavelengths into two and using different scalings for waves with horizontal wavelengths greater than 800 km than for wavelengths less than 800 km. Waves having horizontal wavelengths shorter than 800 km are corrected by the scaling factor developed and validated by *Preusse et al.* [2002, 2003]. Waves having horizontal wavelengths greater than 800 km are corrected for by using a modified scaling containing only the retrieval degradation.

[32] The results for the second CRISTA flight at 25 km altitude are shown as a world map in Figure 3a. The map was calculated by averaging all MF values in a box of 30° longitude and 20° latitude. The box is shifted in steps of 10° longitude and 5° latitude. Each box contains typically 100 single values and only at the very southern latitudes (south of 65°S) are fewer than 50 profiles contained in a box. Please note that the contours are not equidistant to highlight features. The contour levels are chosen to be close together for small values of MF and wider apart for larger values of MF. The contours are 0.7, 1.0, 1.2, 1.4, 1.6, 1.8, 2.0, 2.5, 3.0, 5.0, 10.0, 15.0, 20.0, 25.0 and 30.0.

[33] For comparison we also show the squared GW temperature amplitudes of the same data in Figure 3b. The squared temperature amplitude data are processed in the same way as the MF data. In particular, the same scaling has been applied. Differences between MF and squared amplitude distributions (discussed below) are primarily due to the factor $k_h/m = \lambda_z/\lambda_h$ (Figure 3f) between potential energy and MF in (7) and only slightly affected by synoptic variations of atmospheric temperature and density. Horizontal structures in the ratio λ_z/λ_h are dominated by horizontal structures of the horizontal wavelength as can be seen from maps of the average horizontal wavelength ($\bar{\lambda}_h := 2\pi/\bar{k}_h$) and the average vertical wavelength ($\bar{\lambda}_z$) shown in Figures 3c and 3e.

[34] Extremely high values of MF are observed in the edge of the antarctic polar vortex, where exceedingly high wind speeds of nearly 100 ms^{-1} are found. This correlation of GW activity and wind velocity can be explained by several mechanisms [*Alexander*, 1998; *Preusse et al.*, 2003, 2004]. One explanation is a higher observation probability because a part of the GW spectrum (otherwise invisible to CRISTA) is shifted toward longer vertical wavelength due to high background wind. Another possible reason for high GW activity observed together with high wind speed is that if the GW spectrum is shifted toward longer vertical wavelengths the maximum GW amplitude before the wave becomes statically instable is higher. In the tropics and northern subtropics, patches of high MF are found over the Gulf of Mexico and Central America, and north of the maritime continent along the Chinese and Japanese coast. Typically values there reach ~3 mPa on a regional average. Indications were found that the waves east of China and Japan and above the Gulf of Mexico are generated by deep

convection driven by very high sea surface temperatures (SSTs) [*Preusse et al.*, 2001].

[35] In the tropics there are some regions where waves with very long horizontal wavelengths and high squared amplitudes exist. Prominent regions are south of Hawaii, above South America and north of Madagascar. Although carrying only little MF it would be an interesting topic to find out the nature of these waves.

[36] In particular, in the tropics and subtropics we find the largest differences between Figures 3a and 3b. Figure 3b shows largest values (north of 30°S) in the tropics, the general distribution is nearly symmetric about the equator and the high SST regions in the northern subtropics are only weakly enhanced. In the MF map (Figure 3a) a general northward shift is observed. Nearly all regions of pronounced MF are north of the equator. The MF above the Gulf of Mexico is significantly enhanced and the MF values eastward of China and Japan are the highest found north of 30°S. There is also high MF above the Sahara desert. Although there is no apparent MF source this seems to be a real feature. High GW activity above the Sahara desert has also been found using MLS data [*Jiang et al.*, 2004]. In the edge of the Antarctic polar vortex differences between variances and MF are found, too. In both maps high values of variance and MF show that the GW activity is enhanced above the southern tip of South America and the Antarctic peninsula. However, variances south of South Africa at about 60 south are comparable and cover a larger area (Figure 3b). Obviously, compared to the Antarctic Peninsula, the lower MF values (Figure 3a) in this region are due to very large horizontal wavelength waves which carry less momentum.

4.2. Aliasing

[37] We have observed that some regions of high GW activity are amplified because of their short horizontal wavelengths when calculating MF. This suggests that they are further enhanced if aliasing is taken into account. Effects of aliasing have been discussed by *Preusse et al.* [2002] and in the first part of section 4 for a case study of mountain waves above the Andes showing that MF was underestimated according to (7) by a factor of 3 in this particular case. In general, we cannot infer the true wavelength of singular wave events. We should, however, estimate the aliasing effects on an ensemble average to correct for them and to estimate the resulting uncertainties.

[38] As discussed in section 3, the shapes of the wavelength histograms (Figure 2) indicate different degrees of aliasing. At high northern latitudes the distribution shows that the majority of waves seem to have wavelengths below the Nyquist wavelength, whereas in the tropics the distribution is dominated by long wavelength waves and so is well resolved by the CRISTA sampling. Figure 3c shows corresponding mean horizontal wavelengths close to the random-average wavelength $\breve{\lambda}_h$ at northern latitudes and of about twice this value ($2\breve{\lambda}_h$) in the tropics, respectively. The southern midlatitudes represent an intermediate state both for aliasing (Figure 2c) and for average horizontal wavelength (Figure 3c).

[39] This motivates us to parameterize the degradation of MF due to aliasing by introducing a factor α, which depends on the average horizontal wavelength $\bar{\lambda}_h$ shown in Figure 3c. For average horizontal wavelengths $\bar{\lambda}_h$ larger than or equal to twice the random-average $2\breve{\lambda}_h$ we assume that MF values are calculated correctly ($\alpha = 1.0$). If the average horizontal wavelength $\bar{\lambda}_h$ is equal to the random-average $\breve{\lambda}_h$, this indicates that nearly all wave events are aliased from the spectral range below the Nyquist wavelength and we adopt a maximum factor α_{max}. For horizontal wavelengths between $\breve{\lambda}_h$ and $2\breve{\lambda}_h$ we linearly interpolate α in $\bar{\lambda}_h$. Since the measurements provide no information about the spectral shape below the Nyquist wavelength, and since MF is linear in k_h (see equation (7)), we use the most simple way of estimating α_{max}:

$$\alpha_{max} = \frac{k^*}{\breve{k}_h}. \tag{8}$$

The value k^* used to calculate the value α_{max} is the average horizontal wavenumber of the true spectrum we cannot resolve due to the sparse satellite sampling

$$k^* = \frac{\int_{k_1}^{k_2} I(k)k\,dk}{\int_{k_1}^{k_2} I(k)\,dk} \tag{9}$$

where $I(k)$ is a spectral shape we have to assume. To estimate α_{max}, the maximum aliasing correction, we calculated k^* for some assumptions of $I(k)$. Using $I(k) = const$ and a range between $k_1 = 2\pi/480$ km (the Nyquist wavenumber due to the CRISTA-2 sampling distance) and $k_2 = 2\pi/100$ km (the observational limit due to the limb geometry) we assume that the whole part of the spectrum observed is in the horizontal wavelength range we cannot resolve and we have a completely flat spectral shape, which both is quite unrealistic. This would result in a value of $\alpha_{max} = 5.8$ as some kind of very upper limit. If we use a more realistic spectrum, for example $I(k) \sim k^{-2}$ and a range between $k_1 = \breve{k}_h = 2\pi/960$ km and $k_2 = 2\pi/100$ km we obtain $\alpha_{max} = 2.5$. Most realistic combinations of spectral shape and wavenumber range result in values α_{max} between 2.5 and 4. To avoid overcorrecting in our MF estimation, we therefore assume a somewhat lower value of $\alpha_{max} = 2$.

[40] The degree of uncertainty due to aliasing effects can directly be seen from the horizontal wavelength map (Figure 3c). Especially regions in purple and dark blue indicate mean horizontal wavelengths below 1200 km, i.e., close to the random-average value of $\breve{\lambda}_h = 960$ km for CRISTA-2. In these regions we have only little information about the real mean horizontal wavelength and the aliasing correction is close to the maximum value $\alpha_{max} = 2$. The aliasing correction is assumed to be linear with the horizontal wavelength λ_h: it is maximum for $\lambda_h < \breve{\lambda}_h = 960$ km and equal to 1 for $\lambda_h > 2\breve{\lambda}_h = 1920$ km.

[41] The MF results including aliasing correction are shown in Figure 3d. Some salient features, such as the subtropical northern hemisphere maxima are further enhanced by applying the aliasing correction. Also structures found in the region of very high MF at latitudes south of 40°S are enhanced. Strikingly, the southern tropics which

Table 1. Overview of Different Error Sources Affecting Absolute Values of Momentum Flux (MF) Shown in Figure 3d[a]

		Error Source	Lower Boundary, %	Upper Boundary, %
4.3.1		Amplitude		
	(1)	Quiet regions	20	0
	(2)	Selection proc.	20	25
	(3)	Scaling fct.	20	160
	(4)	Average of pair	0	8
4.3.2		Vertical wavel.	3	6
4.3.3		Horizont. wavel.		
	(1)	Phase scatter	10	20
	(2)	Aliasing	factor <2	factor <2.5

[a]The labeling numbers (first column) follow the error discussion given in section 4.3 (see also Appendix B). We separately estimate the errors for overestimation and underestimation of the real values and give a realistic lower and upper boundary, respectively. Values given are typical values based on zonal means. For details of the error estimation, see text.

display real maxima of variance (Figure 3b) are minima in MF.

4.3. Discussion of Momentum Flux Errors

[42] In order to compare these values with the momentum balance of the QBO [*Dunkerton*, 1997], with GW parameterization schemes [e.g., *Hines*, 1997; *Warner and McIntyre*, 2001], or with previous experimental estimates [*Alexander et al.*, 2000; *Worthington and Thomas*, 1996], we need to specify the MF error. Our MF estimates are based on amplitude, vertical and horizontal wavelength. All three quantities are uncertain to some degree. We first describe all possible error sources we are aware of. Then we describe how the resulting errors are estimated. The results are summarized in Table 1.

4.3.1. Amplitude

[43] 1. Quiet regions/quiet profiles: In the absence of atmospheric wave events, instrumental noise and detrending errors provide a spurious signal that is interpreted as wave events. In consequence, quiet regions, where fluctuations tend to zero, cannot exist in the data. The result, assuming that there are quiet regions in nature, is higher mean values than would be the case in the absence of instrumental noise and detrending errors.

[44] 2. Selection processes: In order to determine the horizontal wavelength we focused on profile pairs where the vertical wavelength of the single wave events is similar. This constraint is defined by the vertical wavelength difference $\Delta\lambda_z$. However, as shown by *Preusse et al.* [2002], the relative error of the vertical wavelength is approximately constant and hence the absolute error increases with vertical wavelength. The selection process therefore tends to favor short vertical wavelengths, which generally carry lower MF. Thus we might underestimate the MF. On the other hand, if the same wave is present in both profiles of a profile pair it is more likely that one of the profiles is disturbed so that the wave becomes undetectable (for example, by another wave) if the wave amplitude is small. In this case probably the criterion for the vertical wavelength difference would no longer be fulfilled. Therefore a low vertical wavelength difference is more likely to be found for high amplitude waves. Since unequal wave pairs are rejected and not taken into account this underrepresentation of low amplitude waves would bias an average value toward high MF.

[45] 3. Scaling function: As described in section 4.1, retrieved amplitudes are scaled to compensate for degradation due to retrieval and viewing geometry. The dependence of the scaling on horizontal wavelength is taken into account by means of a threshold of 800 km horizontal wavelength (see section 4.1). However, the retrieved wavelength along track available to us might differ from the real horizontal wavelength along line of sight (LOS) relevant for the instrument sensitivity leading to a range of errors from −20% to +160% of MF.

[46] The largest errors correspond to the case of inferred wavelengths along the LOS that are too long which means that the scaling factor multiplying the observed amplitude is too small. The very largest errors of 160% come from the assumption that all the waves with long wavelengths derived actually have short wavelengths and only appear to have long wavelengths due to aliasing or because the wave fronts could be almost parallel to the orbit track and the telescope could view sideward at the same time [*Preusse et al.*, 2002].

[47] The lowest errors correspond to the case of inferred wavelengths along the LOS that are too short. The very lowest errors of −20% result from assuming a sideward viewing telescope with all wave fronts nearly perpendicular to the orbit track at the same time. So too large an amplitude scaling factor would be applied because the wavelength along LOS can be much longer than the wavelength along track. In addition to wrongly deduced horizontal wavelengths, scaling errors due to amplitude growth and geographic location have been taken into account. It should be noted that in future measurements wavelength-induced scaling errors could be eliminated by a finer measuring grid.

[48] 4. Average of pair values: Instead of the two single values in a profile pair a mean amplitude and vertical wavelength is used to evaluate MF.

4.3.2. Vertical Wavelength

[49] In retrieval simulations, *Preusse et al.* [2002] found a vertical wavelength scatter of ±25%. This influences the calculated MF values directly as well as indirectly via the scaling function, which depends on vertical wavelength. Primarily the latter could also influence average values.

4.3.3. Horizontal Wavelength

[50] 1. Phase scatter: As discussed in section 3, phase differences have a random error of ±30°.

[51] 2. Aliasing: Aliasing has been extensively discussed in previous sections.

[52] We address these errors by varying the values inside the error ranges. Zonal mean errors for the error sources described above are listed in Table 1. They show the relative importance of the single error sources. For a detailed discussion, see Appendix B.

[53] In addition to the single value contributions discussed in Appendix B we calculated maps of a conservative upper and lower error limit, respectively, by adopting the error limits of all quantities simultaneously. The lower error limit is about a factor 4 less, the upper error limit is about a factor 5 higher than the best estimate shown in Figure 3d displaying the same salient patterns shown in MF maps, i.e., the considered errors only weakly influence the relative shape. In addition to these large error limits, it should be noted that we can only estimate the MF and the corresponding error of the part of the GW spectrum visible

to CRISTA which does not include the MF carried by waves with horizontal wavelengths shorter than ~100 km.

[54] However, the stated error limits are conservative. For instance, the error induced by scaling is probably overestimated. Also, a more realistic error estimation would use the root-sum-square (RSS) of the individual errors. Furthermore, no indication is found that the salient patterns shown in Figure 3 are caused by the error sources investigated, but very likely the contrast between quiet and enhanced regions is even underestimated as the comparison of Figures 3a and 3d shows.

[55] It is important to note that the major part of the resulting error is due to the uncertainties in horizontal wavelength estimation that arise from limited horizontal sampling of the data considered and hence from aliasing issues. A limb scanning instrument with better horizontal sampling, for example 50 km along and 50 km across the satellite track, would be able to oversample all waves with horizontal wavelengths visible for the limb geometry. In this case it would be possible to determine the horizontal wavelength and propagation direction of all waves properly. The resulting estimates of the error due to aliasing would be zero, the error due to the scaling function would arise only from amplitude growth effects and geographic location of about 20%. This would reduce the overall MF error immediately to better than about 40% and even the direction of the MF vector could be determined. Another significant reduction of the error value could be achieved by, e.g., further improving the retrieval algorithm. Thus a satellite instrument with enhanced horizontal sampling would be a very valuable future instrument as it would allow us to obtain more accurate MF values to validate GW parameterizations used in GCMs.

4.4. Comparison With Other Estimates

[56] Given these large errors for the CRISTA MF estimates, at first sight it might be questionable whether these numbers can give any new insight into the GW MF problem, in particular, since we do not know the propagation direction. However, uncertainties about GW MF in GCMs are huge. A good example is the intercomparison of two GW parameterization schemes by *Charron et al.* [2002]. They tune the source MF of a Hines-type [*Hines*, 1997] and a Warner and McIntyre three-part [*Warner and McIntyre*, 2001] GW parameterization scheme to obtain realistic MF values and dissipation rates in the mesosphere. For one specific propagation direction values at the launch altitude of 4 km of ~1 mPa for the Hines scheme and ~10 mPa for the Warner and McIntyre scheme, respectively, resulted in realistic values in the mesosphere. At 25 km altitude these values are significantly decreased, depending on the background wind profile. The values seen by CRISTA equatorward of 40°S correspond to the highest values found by *Charron et al.* [2002]; the values in the southern polar vortex exceed the simulations by orders of magnitude.

[57] A comparison with other measurements of MF would also be very useful. However, this turns out to be difficult because the range of horizontal and vertical wavelengths covered by satellite measurements is different from the range covered by radar or in situ measurements. Therefore the following examples are provided only for reference.

[58] First we compare the region of enhanced MF east of Asia to in situ measurements taken by NASA's ER-2 aircraft at about 19 km altitude [*Alexander et al.*, 2000], although it should be noted that the two data sets observe a very different range of horizontal wavelength waves. Average MF for waves with horizontal wavelengths 5–150 km measured by the aircraft over deep convective clouds ranged from 50–150 mPa. At 25 km CRISTA shows peak values of 10–30 mPa for single events (i.e., without aliasing correction) with horizontal wavelengths longer than ~100 km.

[59] Midlatitude radar measurements by *Worthington and Thomas* [1996] for altitudes between 4 km and 16 km are of the same magnitude as CRISTA measurements outside the polar vortex. However, it is very difficult to extrapolate to such low altitudes from one single-altitude map.

[60] Furthermore, the enhancements in the polar vortex and those above active convection in the tropics and northern subtropics relative to all other regions in the horizontal maps shown in Figures 3a and 3d are real enhancements of the absolute MF. Whether they are also maxima of the net MF and at which altitudes they might impact the global dynamics of the atmosphere largely depends on the horizontal propagation direction of these waves. Such inferences could be possible by further reasoning, but they are beyond the scope of this paper.

5. Comparison With the Warner and McIntyre GW Parameterization Scheme

5.1. Basics of the Warner and McIntyre GW Parameterization Scheme

[61] For the first time, CRISTA provides a global data set of measured MF, which can be used to investigate how realistic horizontal structures in results of GW parameterization schemes are and how the MF values compare. For this first comparison we use the Warner and McIntyre three-part ultrasimple GW parameterization scheme [*Warner and McIntyre*, 1996, 1999, 2001].

[62] The Warner and McIntyre scheme is a computationally inexpensive GW parameterization intended for use in GCMs. There are some major simplifications to reduce computational cost. First, the model uses the midfrequency approximation of the dispersion relation: $\hat{\omega}^2 = N^2 k_h^2/m^2$ (see equation (3)). This allows the $\hat{\omega}$ dependence to be integrated out, reducing the 3D MF spectrum dependent on $\hat{\omega}$, m and the horizontal direction Φ to a 2D spectrum only dependent on m and Φ. Second, power laws are used for the spectral shapes. The spectrum can be composed from as many as three parts with different spectral powers. The long wavelength part of the vertical wavenumber spectrum is assumed to be proportional to m^s with $s = 1$. The medium and large m part of the vertical wavenumber spectrum are each assumed to be proportional to m^{-t} with $t = 3$. This m^{-3} behavior corresponds to simple models of saturation by wave breaking [*Allen and Vincent*, 1995; *Bacmeister et al.*, 1996].

[63] An MF source distribution is launched from a fixed launch pressure level. This source distribution is about constant in longitudinal direction. There is a latitudinal dependency almost symmetric to the equator of about a factor of 2–3 with low values at the equator and higher values toward the poles. At each grid point the same MF

launch spectrum is used for each of the 4 azimuthal directions. The three-part model then propagates the wave spectrum vertically upward in a column and takes into account the effects of wind filtering and wave dissipation in a semi-empirical approach [*Warner and McIntyre*, 1996, 1999, 2001].

5.2. Comparison With CRISTA Measurements

[64] A comparison between model results and CRISTA measurements has been carried out for the CRISTA-2 period (August 1997). The Warner and McIntyre GW parameterization scheme was run for August 11, 1997 (about the middle of the high horizontal resolution CRISTA-2 measuring period). Runs were made for different wave launch levels from 681.3 hPa to 68.13 hPa using UKMO wind and temperature data. For this first study the model as described by *Warner and McIntyre* [2001] was used without further tuning. The standard MF launch spectrum was taken assuming the power laws described in section 5.1 and the value $m_\star = 2\pi/2$ km for the wavenumber defining the spectral maximum of the vertical wavenumber spectrum at the launch level.

[65] Because the CRISTA data do not allow the calculation of the direction of MF, we estimated absolute values of model MF by adding the squares of the MF components for all 4 directions and then taking the square root, which provides the best comparison to the CRISTA data. Global maps of MF absolute values at 25 km altitude (observation level) were calculated also for model data. At the observation level an observational filter has to be applied to the model results because a limb scanning instrument is only able to observe a limited range of horizontal and vertical wavenumbers. For the CRISTA-2 case due to limb geometry and data processing only GWs with vertical wavelengths between 6 and 30 km and horizontal wavelengths between about 100 and 5000 km are visible.

[66] To give a rough estimate of the amount of MF not visible to CRISTA we can compare unfiltered model results to MF values after applying vertical and horizontal wavelength filtering. Filtering the model results for vertical wavelengths visible for CRISTA lowers the model MF values roughly by a factor of 2. This indicates that there is a fair amount of GW MF at short vertical wavelengths, which has also been found by *Vincent and Alexander* [2000] and *Alexander and Vincent* [2000]. Filtering also for horizontal wavelengths visible for CRISTA in a next step lowers the MF again by about a factor of 2, so this could be an estimate for the fraction of MF at horizontal wavelengths too short to be visible for CRISTA. As a whole CRISTA would be able to observe about 25% of the total GW MF. These statements, however, are based on the assumption that the MF spectrum used in the model is realistic.

[67] Figure 4a shows a global map of absolute values of model MF (see above) at 25 km altitude filtered for vertical and horizontal wavelengths visible for CRISTA. The waves were launched at the pressure level 215.4 hPa. Figure 4b is the same as Figure 4a, but for the launch level 681.3 hPa. The modeled MF results show an equatorial minimum (Figures 4a and 4b) which is also observed in the CRISTA MF results (Figure 3d). At the same time the relative distribution of global temperature variance observed by CRISTA looks quite different showing an equatorial maximum (Figure 3b).

[68] While the global MF distribution in the model run with launch level 215.4 hPa is more or less symmetric to the equator the model results for the 681.3 hPa launch level are very similar to the CRISTA MF results (Figure 3d), showing lower MF values in the northern hemisphere. Although minor shifts may appear even part of the smaller scale structures can be reproduced very well like the shape of the region of high MF at southern latitudes and the regions of enhanced MF in the northern subtropics above the Gulf of Mexico and southeast Asia. However, the CRISTA MF values of Figure 3d are considerably higher. The color scale of Figure 3d is 2 times higher than in Figures 3a and 4b. The color scale of Figure 4a is 2 times lower than in Figures 3a and 4b.

[69] The similarity between Figures 4b and 3d is striking and suggests that tropospheric winds have a strong influence on the MF that reaches the lower stratosphere. The comparison also suggests that variations in the typical horizontal wavelength are important in reducing the MF in the tropics (where the temperature variance is large, but the MF is small). Some enhancements of CRISTA MF found in the northern subtropics or above South America and the Antarctic Peninsula could perhaps be an indication for additional GW sources which are not included in the model (like local maxima of convection or mountain waves).

[70] For a better comparison the global maps at 25 km altitude of several parameterization scheme runs with different launch levels have been correlated with the horizontal MF distribution at 25 km altitude derived from CRISTA-2 data as well as to the CRISTA-2 temperature variance distribution. As a raw measure of comparison Figure 5 gives the correlation coefficients for log-log scatterplots of pairs of global maps at 25 km altitude (always model results versus CRISTA-2 GW MF (black curve) or CRISTA-2 GW squared temperature amplitudes (red curve)).

[71] The single values of the scatterplots are obtained from rectangular boxes sized 30° longitude times 20° latitude (see section 4.1). Only those boxes with more than 100 CRISTA values have been considered to obtain statistically more reliable results. By choosing boxes with more than 100 values some very high values from the southern polar vortex are not considered but this does not change the overall picture.

[72] Obviously for all model launch levels the CRISTA MF values are in much better agreement with the model results than the squared temperature amplitudes are. This indicates that there is some kind of agreement in the vertical to horizontal wavelength ratio between model and the CRISTA data. It is also evident that the runs with the lowest wave launch levels (681.3 hPa and 464.2 hPa) match the CRISTA MF distribution best. This is valuable information since the question which launch level is most appropriate for use in GW parameterizations is still an open issue [*Fritts and Alexander*, 2003].

[73] Figure 6 shows scatterplots of the CRISTA MF distribution at 25 km and the model run with launch level 681.3 hPa (Figures 3d and 4b). In Figure 6a, linear scaling is used for the axes. For comparison, Figure 6b shows the same data using logarithmic scales. There is a kind of linear

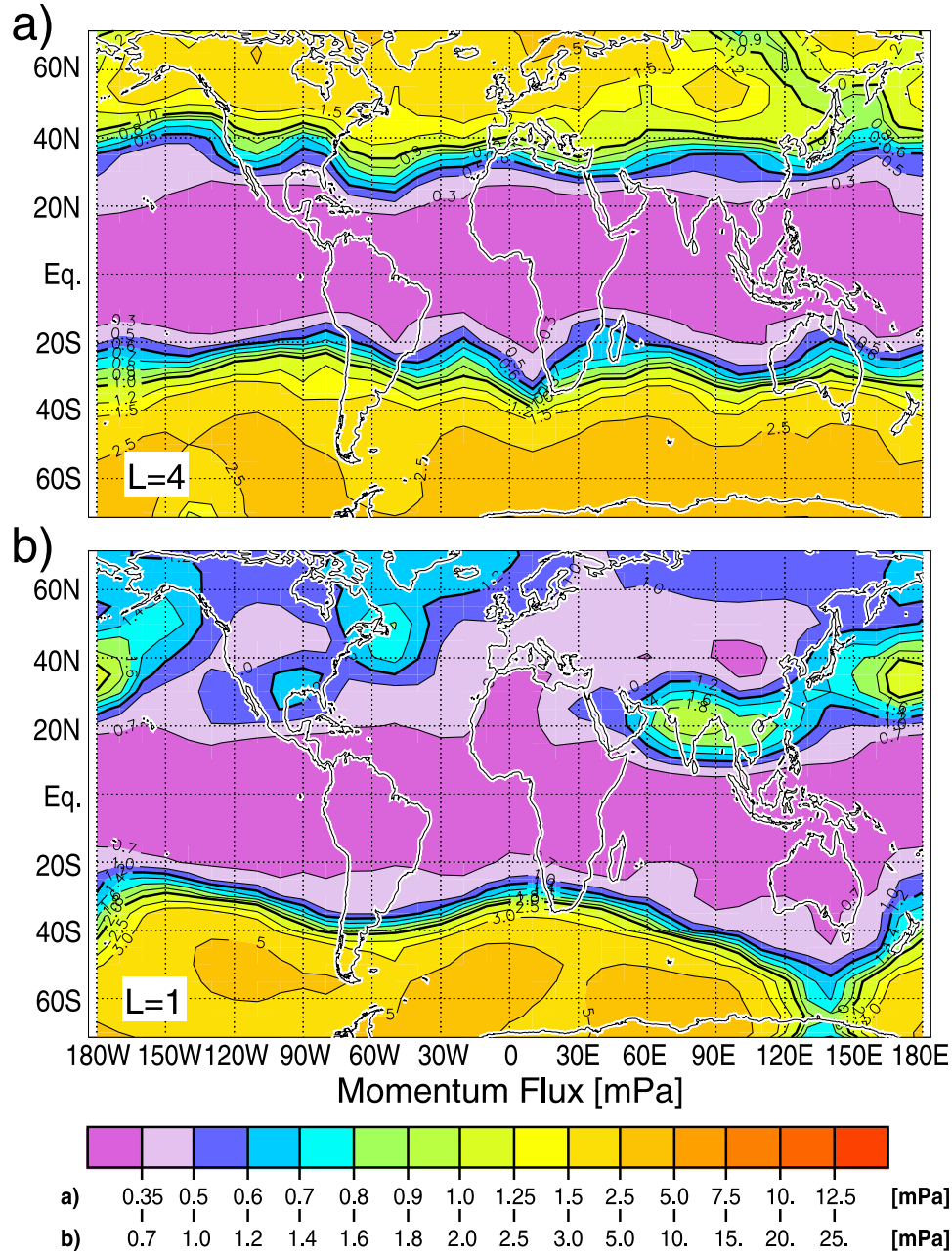

Figure 4. Gravity wave momentum flux (GW MF) at 25 km altitude calculated with the Warner and McIntyre GW parameterization scheme using UKMO winds for August 11, 1997. The waves were launched at the pressure levels (a) 215.4 hPa and (b) 681.3 hPa (UKMO pressure levels L = 4 and L = 1). Values are filtered according to the horizontal and vertical wavelength ranges visible for CRISTA.

relationship between the two data sets although there is a scatter of about a factor of 4 in the data. The straight lines in both Figures 6a and 6b represent the same linear fit through the origin (0, 0) performed on linear scale. The slope is about 2. The log-log diagram is also shown to highlight a discrepancy found at low MF values (x-values below about 0.7 mPa) where values obtained from the parameterization scheme are generally much lower than the CRISTA values. These low values are mainly from the equatorial region. This might be an indication that the standard MF launch distribution taken for the model runs is not adequate for the whole globe. Indeed, enhanced deep convection would be expected in the tropics serving as stronger source for nonorographic gravity waves. On the other hand, part of the discrepancies could also be caused by the approximation we use for the absolute values of the model MF.

[74] It is an amazing fact that a lot of the structures visible in the CRISTA measurements can be explained by sending the standard model launch distribution through a realistic wind field when low model launch levels are used. Obviously the modification of the wave field by the low level winds results in a more realistic horizontal MF distribution above the tropopause. One possible explanation would be

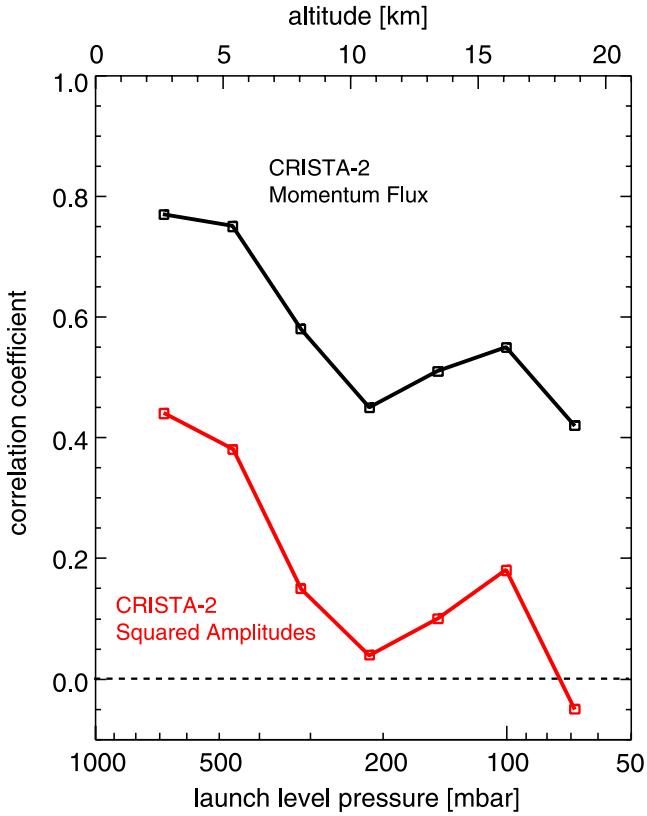

Figure 5. Correlation coefficients for log-log scatterplots of pairs of global maps (model results versus CRISTA-2 (August 1997) gravity wave momentum flux (GW MF) (black curve) or CRISTA-2 squared GW temperature amplitudes (red curve)) at 25 km altitude for different model launch levels.

that in reality there is some kind of global GW source in the atmosphere at low altitudes similar to the standard model launch distribution. However, it is an open question what would be such a low-altitude source mechanism. Another possible explanation would be that GW sources at higher altitudes or larger vertical extent are influenced (modulated) by the wind field in a way that the resulting MF pattern at higher altitudes is very similar to the pattern obtained from wind filtering the standard model launch distribution launched at low levels. Perhaps there are also other possible explanations. However, we cannot decide which explanation is the correct one. Further investigations would be a very interesting topic giving further insight into the mechanisms of GW generation.

[75] Overall, although the magnitudes are different, horizontal structures found in MF derived from CRISTA-2 data and simulations with the Warner and McIntyre parameterization scheme are in very good agreement, in particular, if low wave launch levels are used. This shows the potential to determine source distributions etc. in future work. Thinking of a new generation of limb scanning satellite instruments with even better horizontal resolution than the CRISTA data it would be possible to resolve all waves visible for the limb geometry. Then also the direction of the MF (full MF vectors) could be determined opening a wide field of applications like detailed comparison of the net MF with GCMs.

6. Summary

[76] In this paper we combined the phases provided by the wave analysis of adjacent temperature vertical profiles measured by the CRISTA satellite instrument to estimate the horizontal wavelength of gravity waves (GWs). The along-track phase-difference method proposed in section 3.1 is based on the assumption that the wave-field can be described sufficiently by one leading horizontal wavelength. On this basis only two measuring points from the same wave train are required to estimate a reliable horizontal wavelength. Thus, in a philosophical sense, the proposed analysis method is complementary to standard methods of spectral analysis, which result in a wide spectrum of wavenumbers, but assume that a large region of investigation is covered homogeneously by the same waves (even wavelet analysis does not work for spatial variations of the order of or shorter than the extent of the wavelet). Both requirements, homogeneity as well as monochromacy, are severe. Case studies of mountain waves above South America [*Tan and Eckermann*, 2000; *Preusse et al.*, 2002] revealed gravity wave fields of several hundred kilometers horizontal extent and a dominant horizontal wavelength of 130 km. Due to the sampling distance of 200 km or more these wave events are often captured by three or fewer adjacent data points. In these case studies therefore the assumption that a larger number of sampling points cover a homogeneous wave seems to be much less realistic than the assumption of a dominant horizontal wavelength.

[77] Horizontal wavelengths at mid and high latitudes of the summer hemisphere are very close to the limit given by the horizontal sampling along the satellite track. This is further confirmed by a wavenumber histogram for CRISTA-2 northern high latitudes, displaying a homogeneous wavenumber distribution. This indicates that the horizontal wavelengths of the observed waves are smaller than the Nyquist wavelength.

[78] CRISTA results show that long horizontal wavelength, low-frequency GWs exist in the tropics whereas they are suppressed by the Coriolis force in the mid and high latitudes. This is experimental support for the two mechanisms proposed by *Alexander et al.* [2002] to explain the tropical maximum observed in satellite climatologies of GW variances. First, long horizontal wavelength/low-frequency GWs are expected to be more dominant at low latitudes because of the $\hat{\omega}^{-p}$ dependency of the GW energy spectrum. Second, observation probability is higher for this type of waves.

[79] At present there is little information about the global distribution of GW momentum flux (MF). This, however, is a major point of interest since GW MF greatly influences the background state of the middle atmosphere. Simultaneous retrieval of amplitude, vertical and horizontal wavelength of individual waves provides sufficient information to calculate GW MF. However, since a large number of waves have horizontal wavelength below the Nyquist wavelength we cannot deduce the propagation direction of the wave and hence we cannot deduce the direction of the MF. We therefore calculate absolute values of MF. A map from data of the second CRISTA flight in August 1997 at 25 km altitude is shown and compared with a variance map of the same data. It is shown that the relative distributions are

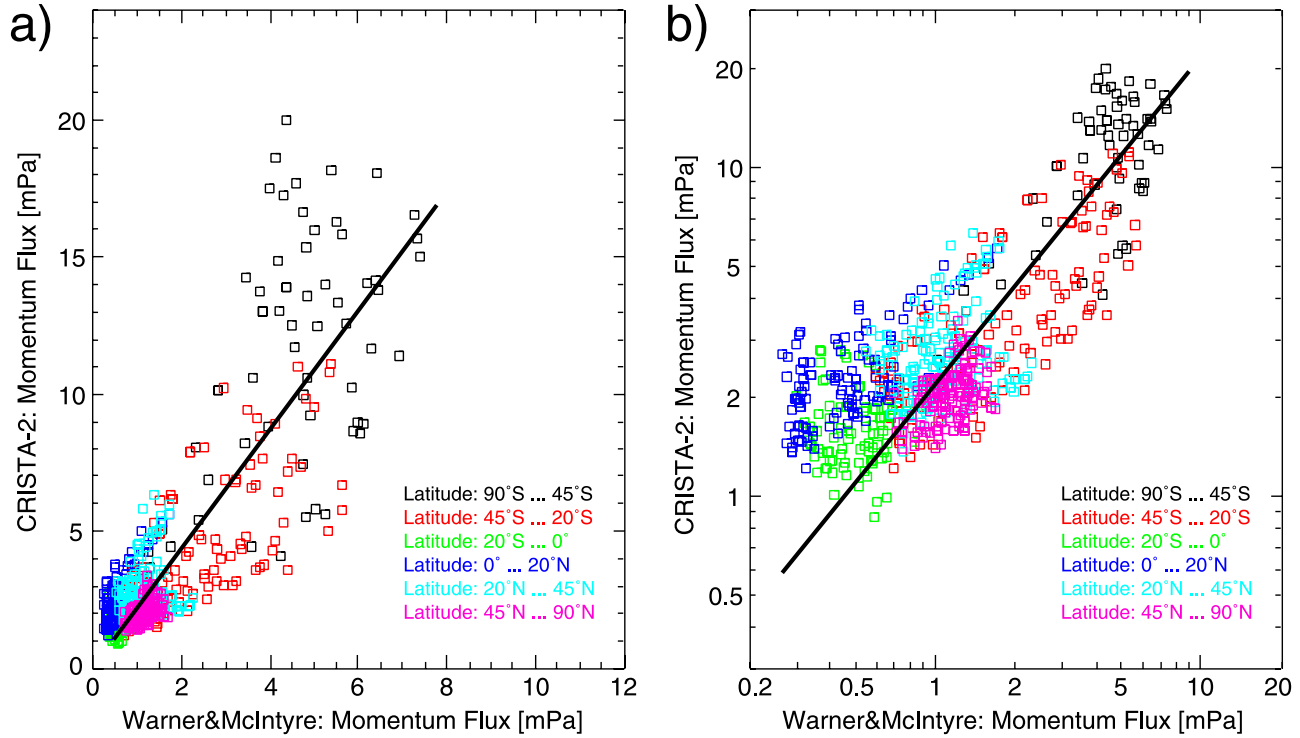

Figure 6. Scatterplots of the horizontal distributions of gravity wave momentum flux (GW MF) at 25 km altitude obtained from CRISTA-2 (August 1997) with aliasing correction applied and from the Warner and McIntyre GW parameterization scheme using UKMO winds for August 11, 1997. The same values and the same linear fit curve through (0, 0) are shown using (a) linear axes and (b) logarithmic axes. The waves were launched at the pressure level 681.3 hPa. The parameterization scheme values are filtered according to the horizontal and vertical wavelength ranges visible for CRISTA.

different. In particular, the northern subtropics are more enhanced and the tropics weaker in the MF map. Also the GW activity in the southern polar vortex displays an internal structure, which is only indicated weakly in the variances. Therefore even absolute values of MF are much better suited for the comparison of GW activity measured and modeled (e.g., in global circulation models) than variances are.

[80] For meaningful comparisons reliable error bars are required. We therefore performed a comprehensive error analysis. The results are summarized in Table 1. The leading error source is the horizontal wavelength, which influences the results via a scaling function compensating the instrument sensitivity (error 4.3.1 (3) in Table 1) as well as via the fact that MF is inversely proportional to horizontal wavelength (equation (7)).

[81] Figure 3c shows that average horizontal wavelength varies with region. Thus also relative distributions of MF are affected, and the contrast between quiet and active regions in Figure 3a is probably underestimated. We therefore developed a simple correction algorithm to account for aliasing effects. Refined MF values shown in Figure 3d indeed show further enhancement of salient features in the northern subtropics and southward of 40°S.

[82] A rough intercomparison between the new CRISTA MF results and previous measurements and modeling shows reasonable agreement. The intercomparison is partly hampered because CRISTA can only detect those waves which have horizontal wavelengths $\lambda_h > 100$ km and because of the different altitudes of the measurements.

[83] A comparison with results of the Warner and McIntyre GW parameterization scheme filtered for the horizontal and vertical wavelength ranges visible for CRISTA shows good agreement between the horizontal distributions. Even some smaller scale structures are reproduced. The best agreement is found for the lowest launch levels of the parameterization scheme. Absolute values of the CRISTA MF are about a factor of 2–4 higher.

[84] Our results demonstrate that the retrieval of GW MF for waves with sufficiently large horizontal wavelengths ($\lambda_h > 100$ km) is possible. Valuable comparisons with GW parameterization schemes can be made, although an important part of the spectrum ($\lambda_h < 100$ km) still remains unresolved. However, the main shortcomings at present are the large errors and the failure to retrieve the direction of MF. Errors could be significantly reduced (see section 4.3) and MF direction retrieved if the horizontal sampling distance were reduced to a grid of 50 km × 50 km or finer across and along the orbit track of the satellite in future missions.

Appendix A: Calculation of the Vertical Flux of Horizontal Momentum

[85] In this section, equation (6) will be derived. We start from equation (41) in *Fritts and Alexander* [2003]

$$(F_{px}, F_{py}) = \bar{\varrho}\left(1 - \frac{f^2}{\hat{\omega}^2}\right)(\overline{u'w'}, \overline{v'w'}) \qquad \text{(A1)}$$

valid for conservative propagation of the waves. The vector (u', v', w') is the vector of wind perturbations. The bar above the products of the wind perturbations indicates the time average over a full period.

[86] The gravity wave solutions are assumed to have the form of equation (14) in *Fritts and Alexander* [2003]

$$\left(u', v', w', \frac{\Theta'}{\bar{\Theta}}, \frac{p'}{\bar{p}}, \frac{\varrho'}{\bar{\varrho}}\right) = \left(\tilde{u}, \tilde{v}, \tilde{w}, \tilde{\Theta}, \tilde{p}, \tilde{\varrho}\right) \times \exp\left[i(kx + ly + mz - \omega t) + \frac{z}{2H}\right] \quad \text{(A2)}$$

with pressure p, potential temperature Θ and the ground relative frequency ω. The bar indicates the values of the atmospheric background state, the prime indicates the perturbation values.

[87] If we explicitly write down the time average using the real parts of the wind perturbations, the component F_{px} from equation (A1) can be rewritten in the form:

$$F_{px} = \bar{\varrho}\left(1 - \frac{f^2}{\hat{\omega}^2}\right)\frac{1}{\tau}\int_0^{\tau} Re\{u'\}Re\{w'\}dt \quad \text{(A3)}$$

with $\omega = 2\pi/\tau$. This can also be done for F_{py}.

[88] The wind perturbations u' and w' can be inserted using equation (A2). This way we obtain

$$F_{px} = \bar{\varrho}\left(1 - \frac{f^2}{\hat{\omega}^2}\right) \times \frac{1}{2} Re\left\{\tilde{u}\tilde{w}^* e^{z/H}\right\} \quad \text{(A4)}$$

with $\tilde{w}^*$ being the complex conjugate of $\tilde{w}$. Then we make use of the polarization relations:

$$-i\hat{\omega}\tilde{\Theta} + (N^2/g)\tilde{w} = 0 \quad \text{(A5)}$$

$$\tilde{p} = \left(\frac{\hat{\omega}^2 - f^2}{\hat{\omega}k + ifl}\right)\tilde{u} = \left(\frac{\hat{\omega}^2 - f^2}{\hat{\omega}l - ifk}\right)\tilde{v} \quad \text{(A6)}$$

(equations (18) and (27) in *Fritts and Alexander* [2003]). In addition, from equations (17), (18) and (20) in *Fritts and Alexander* [2003] we also obtain:

$$\tilde{w} = \frac{-\hat{\omega}}{N^2 - \hat{\omega}^2}\left(m + i\left(\frac{1}{2H} - \frac{g}{c_s^2}\right)\right)\tilde{p} \quad \text{(A7)}$$

where c_s is the sound speed and g is the gravity acceleration.

[89] Inserting equations (A5), (A6), and (A7) in equation (A4), the amplitudes $\tilde{u}$ and $\tilde{w}$ can be replaced by $\tilde{\Theta}$, resulting in

$$F_{px} = -\left[1 - \frac{\hat{\omega}^2}{N^2}\right] \times \left[1 + \frac{1}{m^2}\left(\frac{1}{2H} - \frac{g}{c_s^2}\right)^2\right]^{-1} \times \left[1 + \frac{fl}{mk\hat{\omega}}\left(\frac{1}{2H} - \frac{g}{c_s^2}\right)\right] \times \frac{1}{2}\bar{\varrho}\frac{k}{m}\left(\frac{g}{N}\right)^2 |\tilde{\Theta}|^2 \exp(z/H) \quad \text{(A8)}$$

In the same way we can calculate F_{py}:

$$F_{py} = -\left[1 - \frac{\hat{\omega}^2}{N^2}\right] \times \left[1 + \frac{1}{m^2}\left(\frac{1}{2H} - \frac{g}{c_s^2}\right)^2\right]^{-1} \times \left[1 - \frac{fk}{ml\hat{\omega}}\left(\frac{1}{2H} - \frac{g}{c_s^2}\right)\right] \times \frac{1}{2}\bar{\varrho}\frac{l}{m}\left(\frac{g}{N}\right)^2 |\tilde{\Theta}|^2 \exp(z/H) \quad \text{(A9)}$$

Due to conservative wave propagation there is a term $\exp(z/H)$ compensating the altitude dependence in $\bar{\varrho}$. This term can be dropped because we are only interested in the MF at a fixed altitude.

[90] The total vertical flux of horizontal momentum due to GWs is given by

$$F_{ph} = \sqrt{F_{px}^2 + F_{py}^2} \quad \text{(A10)}$$

With $k_h^2 = k^2 + l^2$ and using equations (A8) and (A9), F_{ph} can be written as follows:

$$F_{ph} = \left[1 - \frac{\hat{\omega}^2}{N^2}\right] \times \left[1 + \frac{1}{m^2}\left(\frac{1}{2H} - \frac{g}{c_s^2}\right)^2\right]^{-1} \times \left[1 + \left(\frac{f}{m\hat{\omega}}\right)^2\left(\frac{1}{2H} - \frac{g}{c_s^2}\right)^2\right]^{1/2} \times \frac{1}{2}\bar{\varrho}\frac{k_h}{m}\left(\frac{g}{N}\right)^2 |\tilde{\Theta}|^2 \quad \text{(A11)}$$

Introducing $\hat{\Theta}$ as the potential temperature amplitude of the GW and $\hat{T}$ as the temperature amplitude we can make use of the relation between temperature and potential temperature

$$|\tilde{\Theta}| = \hat{\Theta}/\bar{\Theta} = \hat{T}/\bar{T} \quad \text{(A12)}$$

and replace $|\tilde{\Theta}|$ in equation (A11) to obtain equation (6). In the final step we change to a more common notation for the background temperature omitting the bar.

Appendix B: Discussion of Single Error Sources

[91] In this section the single error sources described in section 4.3 are discussed in more detail. The single error sources are listed in Table 1. From the values given the relative importance of the single error sources can be seen. In detail we address the single error sources as follows:

[92] Quiet regions/quiet profiles: Single profile analysis (e.g., at Wallops Island, 37.8 N 75.5 W) shows that insufficient detrending can be of the order of 2K, but predominantly affects the long wavelengths. This is in good agreement with the shape and amplitude of the difference between the three CRISTA telescopes [*Ern et al.*, 2003]. Noise is present at all wavelength ranges, but only of the order of 0.5 K. We therefore use an empirical, wavelength-dependent threshold of 0.5 K for wavelengths $\leq$10 km, 3 K at 40 km vertical wavelength and a linear interpolation between 10 km and 40 km wavelength and set all amplitudes below this threshold to zero. In this way we underestimate the background of low amplitude waves. This error

source contributes to the lower error limit (∼−20%, Table 1).

[93] Selection processes: We calculated MF values by applying a very narrow filter ($\Delta\lambda_z$ = 2 km) and without any filtering of vertical wavelength differences $\Delta\lambda_z$ at all. The results show that small $\Delta\lambda_z$ result in small MF. The error of the zonal average amounts to −20%/+25% (Table 1).

[94] Scaling function: As discussed above, scaling can induce an underestimation as well as an overestimation of the retrieved amplitudes. To find the lower error limit, we compensate for retrieval degradation only and long vertical wavelength waves remain nearly unscaled. This is equivalent to the assumption that all waves measured have long horizontal wavelength, i.e., we implicitly assume that the wavelength along LOS is frequently much longer than the wavelength along track. The upper error limit is estimated by employing the scaling function for all waves, assuming that the wavelength along LOS is shorter than the wavelength along track or that short horizontal wavelength waves only appear to have long wavelengths because of aliasing. In addition, we take geographical variations into account by using a scaling factor at the edge of the error range given by *Preusse et al.* [2003]. Although we use a λ_h-sensitive scaling, the resulting error of −20%/+160% (Table 1) is highly asymmetric.

[95] Average of pair values: Averaging the amplitudes first and squaring afterward results in a lower mean value than averaging the variances. The difference can be calculated from the amplitude differences. The resulting error of +8% is very small compared to other error sources.

[96] Vertical wavelength: Because of nonlinearities in the scaling function, a scatter in vertical wavelength might also influence the average value of an ensemble. Furthermore, wave amplitudes in a given geographical region are highly variable [*Preusse et al.*, 2001, 2002]. These variations are amplified when squared amplitudes or MF values are considered. A regional average therefore often depends primarily on a few large amplitude values. Thus a random error affecting these large amplitude data points might have a larger effect than the high number (∼100) of data in a given region suggests. Since the basic error source, i.e., the scatter in vertical wavelength, is a random effect we chose Monte Carlo simulation to estimate the resulting error. For each region we calculated 100 mean values based on perturbed vertical wavelengths. For each individual profile we independently modified the vertical wavelength according to an equal distribution in the range ±25% around the original vertical wavelength value. Afterward scaling and MF calculation were performed on the modified data set. To obtain an upper estimate, we calculated the mean plus the standard deviation, and to obtain a lower estimate, we calculated the mean minus the standard deviation of the 100 randomly perturbed ensembles, respectively. The resulting error is of the order of −3%/+6% (Table 1).

[97] Horizontal wavelength, phase scatter: The effect of phase scatter was estimated by an analogous Monte Carlo simulation based on an assumed phase scatter of ±30 degree, resulting in −10%/+20% error (Table 1).

[98] Horizontal wavelength, aliasing: We discussed aliasing in depth in section 4.2, where we rescaled MF based on an underestimation of the maximum correction factor α_{max} = 2. To estimate the corresponding error, we use a large, but realistic value of α_{max} = 4. It should be kept in mind that the resulting error estimate varies with location. For instance, in the southern tropics the error is much smaller.

[99] **Acknowledgments.** Helpful comments by D. Offermann and two anonymous reviewers are gratefully acknowledged. The CRISTA experiment is funded by the Bundesministerium für Bildung und Forschung (BMBF, Berlin) through the Deutsches Zentrum für Luft- und Raumfahrt (DLR, Bonn). This work is partially funded through GSF, Forschungszentrum für Umwelt und Gesundheit GmbH, grant 07ATF14. M. Joan Alexander's work was funded by NASA/ACMAP NASW-01017.

References

Alexander, M. J. (1998), Interpretations of observed climatological patterns in stratospheric gravity wave variance, *J. Geophys. Res.*, *103*, 8627–8640.

Alexander, M. J., and R. A. Vincent (2000), Gravity waves in the tropical lower stratosphere: A model study of seasonal and interannual variability, *J. Geophys. Res.*, *105*, 17,983–17,993.

Alexander, M. J., J. H. Beres, and L. Pfister (2000), Tropical stratospheric gravity wave activity and relationships to clouds, *J. Geophys. Res.*, *105*, 22,299–22,309.

Alexander, M. J., T. Tsuda, and R. A. Vincent (2002), On the latitudinal variations observed in gravity waves with short vertical wavelengths, *J. Atmos. Sci.*, *59*, 1394–1404.

Allen, S. J., and R. A. Vincent (1995), Gravity wave activity in the lower atmosphere: Seasonal and latitudinal variations, *J. Geophys. Res.*, *100*, 1327–1350.

Bacmeister, J. T., S. D. Eckermann, P. A. Newman, L. Lait, K. Chan, M. Loewenstein, M. H. Proffitt, and B. L. Gary (1996), Stratospheric horizontal wavenumber spectra of winds, potential temperature, and atmospheric tracers observed by high-altitude aircraft, *J. Geophys. Res.*, *101*, 9411–9470.

Charron, M., E. Manzini, and C. D. Warner (2002), Intercomparison of gravity wave parameterizations: Hines Doppler-spread and Warner and McIntyre ultrasimple schemes, *J. Meteorol. Soc. Jpn.*, *80*, 335–345.

Dunkerton, T. J. (1997), Role of gravity waves in the quasi-biennial oscillation, *J. Geophys. Res.*, *102*, 26,053–26,076.

Eckermann, S. D., and P. Preusse (1999), Global measurements of stratospheric mountain waves from space, *Science*, *286*, 1534–1537.

Eidmann, G., D. Offermann, and P. Preusse (2001), Fluctuation power spectra in the mid stratosphere at increased horizontal resolution, *Adv. Space Res.*, *27*, 1647–1652.

Eidmann, G., D. Offermann, B. Schaeler, M. Jarisch, and F. J. Schmidlin (2002), Stratospheric variability of temperature and ozone as inferred from the second CRISTA mission: Zonal means and local structures, *J. Geophys. Res.*, *107*(D23), 8180, doi:10.1029/2001JD000721.

Ern, M., D. Offermann, P. Preusse, K. U. Grossmann, and J. Oberheide (2003), Calibration procedures and correction of detector signal relaxations for the CRISTA infrared satellite instrument, *Appl. Opt.*, *42*, 1594–1609.

Fetzer, E. J., and J. C. Gille (1994), Gravity wave variances in LIMS temperatures, I, Variability and comparison with background winds, *J. Atmos. Sci.*, *51*, 2461–2483.

Fritts, D. C., and M. J. Alexander (2003), Gravity wave dynamics and effects in the middle atmosphere, *Rev. Geophys.*, *41*(1), 1003, doi:10.1029/2001RG000106.

Garcia, R. R., and F. Sassi (1999), Modulation of the mesospheric semiannual oscillation by the quasibiennial oscillation, *Earth Planets Space*, *51*, 563–569.

Giorgetta, M. A., E. Manzini, and E. Roeckner (2002), Forcing of the quasi-biennial oscillation from a broad spectrum of atmospheric waves, *Geophys. Res. Lett.*, *29*(8), 1245, doi:10.1029/2002GL014756.

Grossmann, K. U. (2000), Recent improvements in middle atmosphere remote sounding techniques: The CRISTA-SPAS experiment, in *Atmospheric Science Across the Stratopause*, *Geophys. Monogr. Ser.*, vol. 123, edited by D. E. Siskind, S. D. Eckermann, and M. E. Summers, pp. 287–304, AGU, Washington, D. C.

Hines, C. O. (1997), Doppler-spread parameterization of gravity-wave momentum deposition in the middle atmosphere. Part 1: Basic formulation, *J. Atmos. Terr. Phys.*, *59*, 371–386.

Holton, J. R., and M. J. Alexander (2000), The role of waves in the transport circulation of the middle atmosphere, in *Atmospheric Science Across the Stratopause*, *Geophys. Monogr. Ser.*, vol. 123, edited by D. E. Siskind, S. D. Eckermann, and M. E. Summers, AGU, Washington, D. C.

Jiang, J. H., B. Wang, K. Goya, K. Hocke, S. D. Eckermann, J. Ma, D. L. Wu, and W. J. Read (2004), Geographical distribution and interseasonal variability of tropical deep convection: UARS MLS observations and analyses, *J. Geophys. Res.*, *109*, D03111, doi:10.1029/2003JD003756.

Mayr, H. G., J. G. Mengel, and K. L. Chan (1998), Equatorial oscillations maintained by gravity waves as described with the Doppler spread parameterization: I. Numerical experiments, *J. Atmos. Sol. Terr. Phys.*, *60*, 181–199.

McIntyre, M. E. (1998), Breaking waves and global-scale chemical transport in the Earth's atmosphere, with spinoffs for the Sun's interior, *Prog. Theor. Phys.*, *130*, 137–166. (Corrigendum, *Prog. Theor. Phys.*, 1999.)

McLandress, C. (1998), On the importance of gravity waves in the middle atmosphere and their parameterization in general circulation models, *J. Atmos. Terr. Phys.*, *60*, 1357–1383.

McLandress, C., M. J. Alexander, and D. L. Wu (2000), Microwave Limb Sounder observations of gravity waves in the stratosphere: A climatology and interpretation, *J. Geophys. Res.*, *105*, 11,947–11,967.

Medvedev, A. S., and G. P. Klaassen (2000), Parameterization of gravity wave momentum deposition based on nonlinear wave interactions: Basic formulation and sensitivity tests, *J. Atmos. Terr. Phys.*, *62*, 1015–1033.

Offermann, D., K. U. Grossmann, P. Barthol, P. Knieling, M. Riese, and R. Trant (1999), Cryogenic Infrared Spectrometers and Telescopes for the Atmosphere (CRISTA) experiment and middle atmosphere variability, *J. Geophys. Res.*, *104*, 16,311–16,325.

Press, W. H., S. A. Teukolsky, W. T. Vetterling, and B. P. Flannery (1992), *Numerical Recipes in Fortran 77: The Art of Scientific Computing*, 2nd ed., 933 pp., Cambridge Univ. Press, New York.

Preusse, P., B. Schaeler, J. T. Bacmeister, and D. Offermann (1999), Evidence for gravity waves in CRISTA temperatures, *Adv. Space Res.*, *24*, 1601–1604.

Preusse, P., S. D. Eckermann, and D. Offermann (2000), Comparison of global distributions of zonal-mean gravity wave variance inferred from different satellite measurements, *Geophys. Res. Lett.*, *27*, 3877–3880.

Preusse, P., G. Eidmann, S. D. Eckermann, B. Schaeler, R. Spang, and D. Offermann (2001), Indications of convectively generated gravity waves in CRISTA temperatures, *Adv. Space Res.*, *27*, 1653–1658.

Preusse, P., A. Dörnbrack, S. D. Eckermann, M. Riese, B. Schaeler, J. T. Bacmeister, D. Broutman, and K. U. Grossmann (2002), Space-based measurements of stratospheric mountain waves by CRISTA: 1. Sensitivity, analysis method, and a case study, *J. Geophys. Res.*, *107*(D23), 8178, doi:10.1029/2001JD000699.

Preusse, P., S. D. Eckermann, M. Ern, F. J. Schmidlin, M. J. Alexander, and D. Offermann (2003), Infrared limb sounding measurements of middle atmosphere gravity waves by CRISTA, in *Remote Sensing of Clouds and the Atmosphere VII*, edited by K. P. Schäfer et al., *Proc. SPIE*, *4882*, 134–148.

Preusse, P., M. Ern, K. U. Grossmann, and F. J. Schmidlin (2004), Seasonal variations of gravity wave variance inferred from CLAES, in *Remote Sensing of Clouds and the Atmosphere VIII*, edited by K. P. Schäfer et al., *Proc. SPIE*, *5235*, 288–297.

Riese, M., R. Spang, P. Preusse, M. Ern, M. Jarisch, D. Offermann, and K. U. Grossmann (1999), Cryogenic Infrared Spectrometers and Telescopes for the Atmosphere (CRISTA) data processing and atmospheric temperature and trace gas retrieval, *J. Geophys. Res.*, *104*, 16,349–16,367.

Salby, M. L. (1983), Sampling theory for asynoptic satellite observations. Part I: Space-time spectra, resolution, and aliasing, *J. Atmos. Sci.*, *82*, 2577–2600.

Scaife, A. A., N. Butchart, C. D. Warner, D. Stainforth, W. Norton, and J. Austin (2000), Realistic quasi-biennial oscillations in a simulation of the global climate, *Geophys. Res. Lett.*, *27*, 3481–3484.

Tan, K. A., and S. D. Eckermann (2000), Numerical simulations of mountain waves in the middle atmosphere over the southern Andes, in *Atmospheric Science Across the Stratopause*, *Geophys. Monogr. Ser.*, vol. 123, edited by D. E. Siskind, S. D. Eckermann, and M. E. Summers, pp. 311–318, AGU, Washington, D. C.

Tsuda, T., M. Nishida, C. Rocken, and R. H. Ware (2000), A global morphology of gravity wave activity in the stratosphere revealed by the GPS occultation data (GPS/MET), *J. Geophys. Res.*, *105*, 7257–7273.

Vincent, R. A., and M. J. Alexander (2000), Gravity waves in the tropical lower stratosphere: An observational study of seasonal and interannual variability, *J. Geophys. Res.*, *105*, 17,971–17,982.

Warner, C. D., and M. E. McIntyre (1996), On the propagation and dissipation of gravity wave spectra through a realistic middle atmosphere, *J. Atmos. Sci.*, *53*, 3213–3235.

Warner, C. D., and M. E. McIntyre (1999), Toward an ultra-simple spectral gravity wave parameterization for general circulation models, *Earth Planets Space*, *51*, 475–484.

Warner, C. D., and M. E. McIntyre (2001), An ultrasimple spectral parameterization for nonorographic gravity waves, *J. Atmos. Sci.*, *58*, 1837–1857.

Worthington, R. M., and L. Thomas (1996), The measurement of gravity wave momentum flux in the lower atmosphere using VHF radar, *Radio Sci.*, *31*, 1501–1517.

Wu, D. L. (2001), Horizontal wavenumber spectra of MLS radiance fluctuations, *J. Atmos. Sol. Terr. Phys.*, *63*, 1465–1477.

Wu, D. L., and J. W. Waters (1996a), Gravity-wave-scale temperature fluctuations seen by the UARS MLS, *Geophys. Res. Lett.*, *23*, 3289–3292.

Wu, D. L., and J. W. Waters (1996b), Satellite observations of atmospheric variances: A possible indication of gravity waves, *Geophys. Res. Lett.*, *23*, 3631–3634.

Wu, D. L., and J. W. Waters (1997), Observations of gravity waves with the UARS Microwave Limb Sounder, in *Gravity Wave Processes: Their Parameterization in Global Climate Models*, *NATO ASI Ser. I*, vol. 50, edited by K. Hamilton, pp. 103–120, Springer-Verlag, New York.

M. J. Alexander, Colorado Research Associates (CoRA), 3350 Mitchell Lane, Boulder, CO 80301, USA. (alexand@cora.nwra.com)

M. Ern and P. Preusse, Institute for Chemistry and Dynamics of the Geosphere (ICG), Institute I: Stratosphere, Forschungszentrum Jülich, D-52425 Jülich, Germany. (m.ern@fz-juelich.de)

C. D. Warner, Centre for Atmospheric Sciences, University of Cambridge, Wilberforce Road, Cambridge CB3 0WA, UK. (c.d.warner@damtp.cam.ac.uk)